JACS
JOURNAL OF THE AMERICAN CHEMICAL SOCIETY
Article
pubs.acs.org/JACS

Visible Light Photocatalysis with c-WO_{3-x}/$WO_3 \times H_2O$ Nanoheterostructures In Situ Formed in Mesoporous Polycarbosilane-Siloxane Polymer

Mahdi Seifollahi Bazarjani,*[†] Mirabbos Hojamberdiev,[†,‡] Koji Morita,[†,§] Gangqiang Zhu,[∥] Gennady Cherkashinin,[†] Claudia Fasel,[†] Thomas Herrmann,[†] Hergen Breitzke,[⊥] Aleksander Gurlo,[†] and Ralf Riedel[†]

[†]Fachbereich Material-und Geowissenschaften, Technische Universität Darmstadt, Petersenstraße 32, 64287 Darmstadt, Germany

[‡]Materials and Structures Laboratory, Tokyo Institute of Technology, 4259 Nagatsuta, Midori, Yokohama, 226-8502 Kanagawa, Japan

[§]Advanced Ceramics Group, National Institute for Materials Science (NIMS), 305-0047 Tsukuba, Japan

[∥]School of Physics and Information Technology, Shaanxi Normal University, 710062 Xi'an, China

[⊥]Eduard-Zintl-Institut für Anorganische und Physikalische Chemie, Technische Universität Darmstadt, Petersenstraße 20, 64287 Darmstadt, Germany

S *Supporting Information*

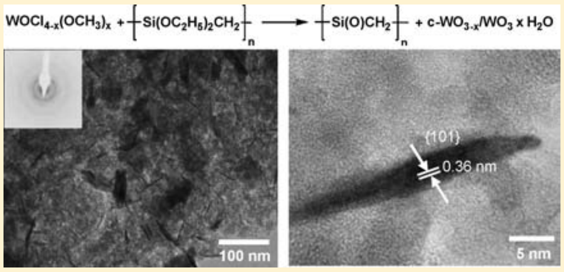

ABSTRACT: In recent years, there have been significant efforts to find novel photocatalytic materials with improved properties. Thus, there is an active ongoing search for new materials that can operate at a broad range of wavelengths for photocatalytic reactions. Among photocatalytically active semiconductors, considerable attention has been given to tungsten oxide with a band gap of $E_g \approx 2.6$ eV, which provides the opportunity to harvest visible light. In the present work, we report on a one-step synthesis of c-WO_{3-x}/$WO_3 \times H_2O$ nanowhiskers dispersed in a hydrolytically stable mesoporous polycarbosilane-siloxane ($[-Si(O)CH_2-]_n$) matrix. The as-synthesized nanocomposites possess high photocatalytic activity for the degradation of methylene blue (MB) under visible light irradiation. The enhanced photocatalytic activity is due to (i) the reduction in the electron−hole recombination rate because of the reduced dimensions of nanowhiskers, (ii) more efficient consumption of photogenerated electrons and holes as a result of the high surface-to-bulk-ratio of the nanowhiskers, and (iii) better electron−hole pair separation due to the formation of c-WO_{3-x}/$WO_3 \times H_2O$ nanoheterostructures.

INTRODUCTION

Semiconductor nanoparticles with high photocatalytic activity and strong quantum-size effect are considered to be superior photocatalysts.[1−4] However, the application of nanoparticles for photocatalytic water decontamination faces several obstacles, including aggregation of nanoparticles and separation/reuse of nanoparticles from photoreactors.[3] The former leads to the rapid loss of active sites and photocatalytic efficiency;[3] the latter results in the contamination of water sources with nanoparticles.[3,5−7] Both are formidable obstacles to green applications.

The above problems have been addressed by the following methods:[3] (i) thin films comprised of meso-/macroporous photocatalysts supported on substrates,[8−12] (ii) photocatalytic nanoparticles supported on porous solids,[13−16] and (iii) photocatalysts supported on membranes for water purification.[17−20]

Here, we implement the second approach to synthesize novel mesoporous nanocomposites, possessing high photocatalytic activity under visible light. A case study includes the design, in situ synthesis, and characterization of nanoheterostructures of cubic tungsten oxide and tungsten oxide monohydrate (c-WO_{3-x}/$WO_3 \times H_2O$) dispersed in a mesoporous polycarbosilane-siloxane matrix.

The reason we work with the c-WO_{3-x}/$WO_3 \times H_2O$ and polycarbosilane-siloxane polymer system is as follows:

TiO_2 is the most widely studied photocatalyst with a band gap (E_g) of ~3.2 eV, which limits the photocatalytic activity of TiO_2 to ultraviolet range.[13,16,21,22] In contrast, crystalline WO_3 with a narrower band gap (e.g., $E_g \approx 2.6$ eV for monoclinic WO_3 in bulk form at room temperature)[2] provides the opportunity to harvest visible light.[2,23,24] WO_3 has been used for the photocatalytic degradation of organic molecules, such as methylene blue and methanol under visible light irradiation.[12,23] However, pure WO_3 is not an efficient photocatalyst because of its relatively low conduction band level (0.5 V vs NHE, normal hydrogen electrode). Therefore, photogenerated

Received: December 28, 2012
Published: February 19, 2013

electrons are not effectively consumed in oxygen reduction reactions, and the subsequent oxidative degradation of pollutants by the holes is hindered.[25−27] Two approaches have been applied to enhance the photocatalytic activity of WO_3.

The first approach focuses on the synthesis of nanostructured WO_3, with tailored morphology,[8,23,28−30] and size.[15,31] Nanostructured WO_3 offers more sites for photocatalytic reactions and reduced diffusion distances for the photogenerated electrons and holes to reaction sites.[2]

In the second method, the photocatalytic efficiency is enhanced by modifying WO_3. Several methods have been suggested to modify WO_3, such as coupling with other semiconductors,[21,25,32,33] noble metals,[26,27,34] and graphene oxide,[35] as well as doping with metal ions[36−38] and non metals.[39,40] For example, coupling of WO_3 with several semiconductors has been reported, and the resultant heterostructures show efficient separation of electrons and holes, leading to an enhanced photocatalytic activity.[21,25,32,33] Cubic tungsten oxide and tungsten oxide hydrate particles provide a heterostructure, resulting in a high photocatalytic activity.[32]

For both approaches, high crystallinity is required because defects are scattering centers and retard the transport of carriers.[23,41] In addition, amorphous WO_3 manifests poor structural and chemical stability.[42] The most distorted structure of amorphous WO_3 has E_g of ~3.25 eV,[2] while E_g of monoclinic WO_3 is ~2.6 eV.[2,41] High annealing temperatures are required to obtain well crystalline WO_3, leading to a considerable decrease in surface area and active sites for photocatalytic reactions.[23]

Mesoporous silica, a typical porous matrix for immobilizing nanoparticles,[15] suffers from inherent poor hydrolytic stability.[43,44] The development of a novel approach to disperse tungsten oxide and/or tungsten oxide hydrate nanoparticles in a hydrolytically stable matrix is required. The hydrolytic stability of silica is significantly enhanced if moisture-sensitive silicon−oxygen bonds (Si−O−Si) are replaced by more stable silicon−carbon bonds ($Si-CH_2-Si$ or $Si-CH_2-CH_2-Si$).[45] This approach was successfully employed for obtaining hydrothermally stable silica membranes[46] and mesoporous organosilicates.[43]

In the present study, we apply a combination of different approaches to in situ synthesize nanoheterostructures of c-$WO_{3-x}/WO_3 \times H_2O$ in the polycarbosilane-siloxane matrix with high surface area at an annealing temperature as low as 120 °C.

SYNTHESIS METHOD

Polycarbosilane-siloxane hybrid polymer ($[-Si(O)CH_2-]_n$) was synthesized, using the procedure given by Liu et al.[47] Accordingly, polydiethoxy carbosilane was gelated in methanol by a 1 M HCl aqueous solution (Scheme 1(I)). $WO_3 \times H_2O$ nanowhiskers were synthesized from tungsten(VI) oxychloromethoxide by applying a similar procedure (Scheme 1(II)). The homogeneous transparent solution of polydiethoxy carbosilane and tungsten(VI) oxychloromethoxide in methanol then was gelated under the same conditions to obtain c-$WO_{3-x}/WO_3 \times H_2O/[-Si(O)CH_2-]_n$ nanocomposite, which consisted of 30 wt % nanowhiskers dispersed in the polycarbosilane-siloxane matrix (Scheme 1(III)).

The concentration of the nanowhiskers (30 wt %) was chosen so as to obtain a mesoporous nanocomposite with no residual microporosity, which was considered to be appropriate for the efficient diffusion of bulky molecules, such as methylene blue (MB) in the pores (for further discussions, refer to Figure S1, Figure S2, Table S1, and the section about porosity optimization in the Supporting Information). Finally, all materials after aging and drying were heat treated under Ar atmosphere at 120 °C (the temperature of tungsten oxide monohydrate formation).[48]

Scheme 1. Schematic Representation of the Synthesis of $[-Si(O)CH_2-]_n$ (I), $WO_3 \times H_2O$ (II), and c-$WO_{3-x}/WO_3 \times H_2O/[-Si(O)CH_2-]_n$ (III) Specimens

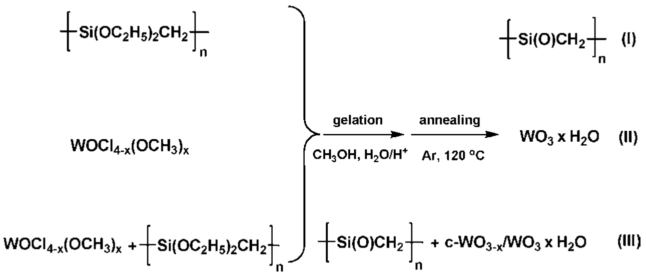

The thermal stability of the $WO_3 \times H_2O$ and c-$WO_{3-x}/WO_3 \times H_2O/[-Si(O)CH_2-]_n$ specimens was analyzed by heat treatment at 200 °C under Ar atmosphere, producing c-WO_{3-x} and c-$WO_{3-x}/[-Si(O)CH_2-]_n$ materials, respectively.

RESULTS AND DISCUSSION

Phase Composition and Microstructure. The X-ray diffraction (XRD) patterns (Figure 1) confirm the formation of orthorhombic tungsten oxide monohydrate ($WO_3 \times H_2O$, space group *Pmnb*, No. 62, $Z = 4$, $a = 5.2477$ Å, $b = 10.7851$ Å, $c = 5.1440$ Å) in the $WO_3 \times H_2O$ and c-$WO_{3-x}/WO_3 \times H_2O/[-Si(O)CH_2-]_n$ specimens (Figure 1b and c, respectively). However, a careful study of the XRD pattern in the c-$WO_{3-x}/WO_3 \times H_2O/[-Si(O)CH_2-]_n$ nanocomposite indicates a re-

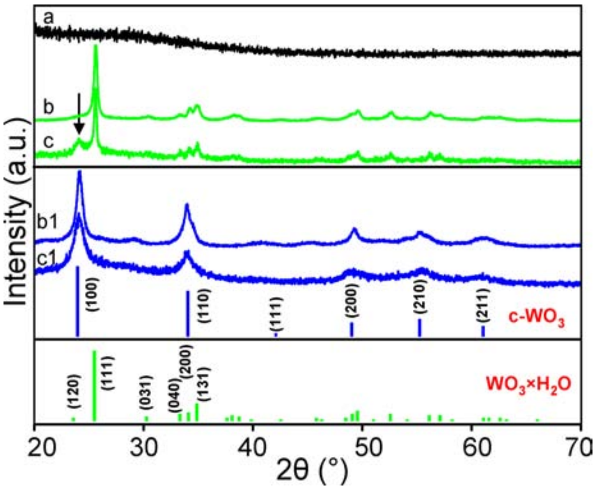

Figure 1. XRD patterns of $[-Si(O)CH_2-]_n$ (a), $WO_3 \times H_2O$ (b), and c-$WO_{3-x}/WO_3 \times H_2O/[-Si(O)CH_2-]_n$ (c) specimens thermally treated at 120 °C. The latter two specimens transform after heat treatment at 200 °C under Ar atmosphere into c-WO_{3-x} (b1) and c-$WO_{3-x}/[-Si(O)CH_2-]_n$ (c1), respectively. At the bottom the diffraction patterns of orthorhombic tungsten oxide monohydrate ($WO_3 \times H_2O$, *Pmnb*, No. 62, $Z = 4$, $a = 5.2477$ Å, $b = 10.7851$ Å, $c = 5.1440$ Å) and cubic tungsten oxide (c-WO_3, $Pm\bar{3}m$, No. 221, $Z = 1$, $a = 3.714$ Å) are shown.

flection (shown with an arrow in Figure 1c), which is attributed to cubic tungsten oxide (c-WO_3, space group $Pm\bar{3}m$, No. 221, $Z = 1$, $a = 3.714$ Å).[32] As to be discussed later, the formed cubic tungsten oxide is substoichiometric (c-WO_{3-x}), and it generates c-WO_{3-x}/WO_3×H_2O nanoheterostructures in the c-WO_{3-x}/WO_3×H_2O/[−Si(O)CH_2−]$_n$ nanocomposite. The specimens, which are heat treated at 200 °C under Ar atmosphere, exhibit the diffraction patterns of cubic tungsten oxide (Figure 1b1 and c1).

High-resolution transmission electron microscopy (HRTEM) characterization confirms the phase composition and crystallinity of the samples, indicating tungsten oxide monohydrate nanowhiskers in the WO_3×H_2O (Figure 2c and d) and c-WO_{3-x}/WO_3×H_2O/[−Si(O)CH_2−]$_n$ specimens (Figure 2e and f). The interplanar d spacing of 0.35 nm is in good agreement with that of the (010) plane of tungsten oxide monohydrate in the WO_3×H_2O specimen. The d spacing of 0.36 nm is in agreement with that of the tungsten oxide monohydrate {101} planes in the c-WO_{3-x}/WO_3×H_2O/[−Si(O)CH_2−]$_n$ nanocomposite. It can also be seen from the TEM study that the [−Si(O)CH_2−]$_n$ hybrid polymer is completely amorphous (see Figure 2a and b).

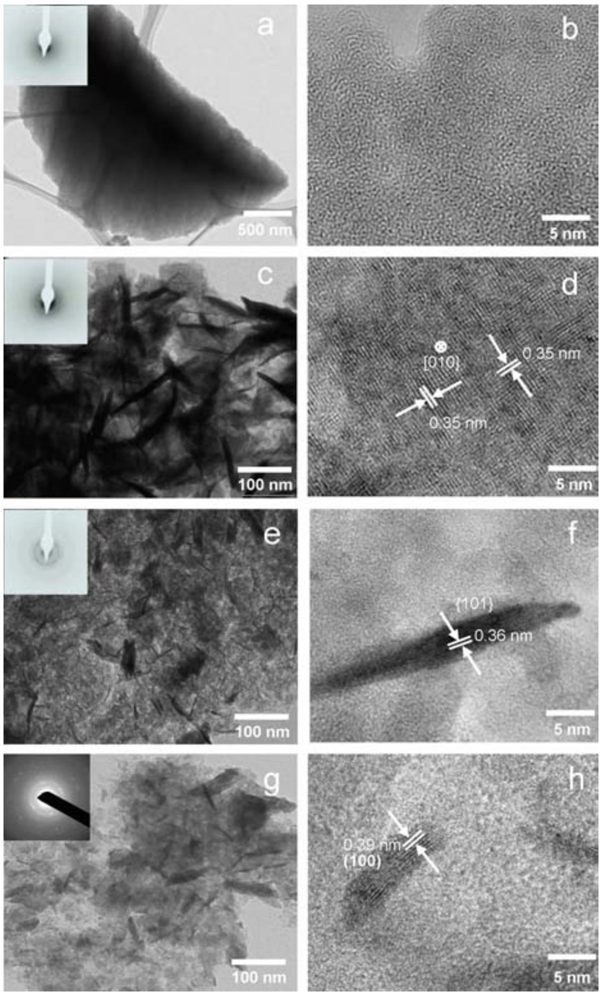

Figure 2. TEM (a,c,e,g) and HRTEM (b,d,f,h) micrographs of [−Si(O)CH_2−]$_n$ (a,b), WO_3×H_2O (c,d), c-WO_{3-x}/WO_3×H_2O/[−Si(O)CH_2−]$_n$ (e,f), and c-WO_{3-x}/[−Si(O)CH_2−]$_n$ (g,h) specimens with the corresponding selected area electron diffraction patterns (insets), which confirm the amorphous character of the polycarbosilane-siloxane hybrid polymer (a), the crystallinity of the nanowhiskers (c,e,g), and the formation of cubic tungsten oxide (h).

The nanowhiskers are ~3 times smaller in the c-WO_{3-x}/WO_3×H_2O/[−Si(O)CH_2−]$_n$ nanocomposite {(5−15) × (20−100) nm^2} as compared to those in the WO_3×H_2O specimen {(20−50) × (100−300) nm^2}. This finding supports the stabilization effect of the polycarbosilane-siloxane matrix, which prevents the growth and agglomeration of the nanowhiskers. The simultaneous formation of the c-WO_{3-x}/WO_3×H_2O nanowhiskers and [−Si(O)CH_2−]$_n$ matrix assures the good dispersion of the inorganic semiconducting nanowhiskers confirmed by the elemental (W, O) mapping (Figure S5).

The TEM and HRTEM results (Figure 2g and h) of the c-WO_{3-x}/[−Si(O)CH_2−]$_n$ nanocomposite show the formation of the cubic tungsten oxide phase and confirm the XRD result (Figure 1c1). The dispersion and size of the nanowhiskers in the c-WO_{3-x}/[−Si(O)CH_2−]$_n$ nanocomposite are homogeneous and similar to those of the c-WO_{3-x}/WO_3×H_2O/[−Si(O)CH_2−]$_n$ nanocomposite. The d spacing of 0.39 nm is slightly larger than that of the cubic WO_3 (100) planes, which could be due to the substoichiometry of the formed cubic tungsten oxide in the c-WO_{3-x}/[−Si(O)CH_2−]$_n$ nanocomposite.

Thermal Stability. Simultaneous thermal analysis coupled with infrared spectroscopy (STA-IR) measurement is performed under Ar atmosphere to study the thermal stability of the c-WO_{3-x}/WO_3×H_2O/[−Si(O)CH_2−]$_n$ nanocomposite (Figure 3).

H_2O and ethene (C_2H_4) are the main gaseous species detected by the STA-IR measurement up to 300 °C. The evolution patterns of the gaseous H_2O and C_2H_4 indicate significant differences between the decomposition behaviors of the [−Si(O)CH_2−]$_n$ hybrid polymer and c-WO_{3-x}/

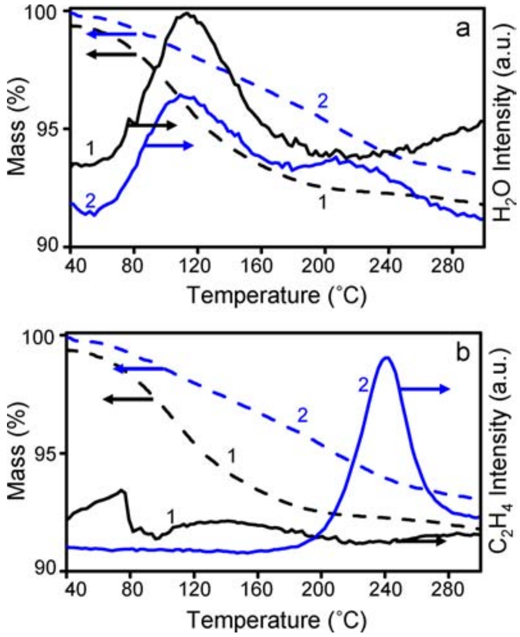

Figure 3. STA-IR measurements showing the mass loss (dashed lines, primary Y axis) of [−Si(O)CH_2−]$_n$ (black, 1) and c-WO_{3-x}/WO_3×H_2O/[−Si(O)CH_2−]$_n$ (blue, 2) specimens during thermolysis under Ar atmosphere. The evolution patterns (solid lines, secondary Y axis) of the gaseous H_2O (a) and C_2H_4 (b) are drawn from the integration of selected IR bands ranges along the temperature profile.

$WO_3{\times}H_2O/[-Si(O)CH_2-]_n$ nanocomposite during the thermolysis: (a) The evolution of H_2O during the thermolysis shows a maximum at ~112 °C in both samples and an additional maximum at ~205 °C in the c-$WO_{3-x}/WO_3{\times}H_2O/[-Si(O)CH_2-]_n$ nanocomposite (Figure 3a). The first maximum at ~112 °C is related to the evaporation of adsorbed water in pores. The second maximum at ~205 °C in the c-$WO_{3-x}/WO_3{\times}H_2O/[-Si(O)CH_2-]_n$ nanocomposite is associated with the dehydroxylation of the tungsten oxide monohydrate to the cubic tungsten oxide. (b) The release of C_2H_4 from the c-$WO_{3-x}/WO_3{\times}H_2O/[-Si(O)CH_2-]_n$ nanocomposite starts at ~190 °C and has a maximum at ~240 °C, while C_2H_4 does not outgas from the pure $[-Si(O)CH_2-]_n$ specimen (Figure 3b). The evolution of C_2H_4 from the c-$WO_{3-x}/WO_3{\times}H_2O/[-Si(O)CH_2-]_n$ nanocomposite is related to rearrangement reactions.[47] The rearrangement reactions are facilitated by the oxygen transfer (loss) from WO_3 to carbosilane bonds ($Si-CH_2-Si$), leading to the formation of WO_{3-x} and silicon−oxygen bonds ($Si-O-Si$), respectively, as well as release of C_2H_4 (combination of $-CH_2-$ linkages). Hence, the nanowhiskers facilitate the decomposition of $[-Si(O)CH_2-]_n$ matrix at temperatures as low as 200 °C.

Optical Properties and Surface Composition. Diffuse reflectance UV−vis (DR-UV−vis) spectroscopy reveals that the band gap (E_g) of the c-$WO_{3-x}/WO_3{\times}H_2O/[-Si(O)CH_2-]_n$ nanocomposite is ~2.54 eV, which is slightly larger than $E_g \approx 2.49$ eV of the $WO_3{\times}H_2O$ specimen (Figure 4a, inset, refer to the Supporting Information for the details of the calculations). This difference is explained by the smaller particle size in the c-$WO_{3-x}/WO_3{\times}H_2O/[-Si(O)CH_2-]_n$ nanocomposite as compared to the $WO_3{\times}H_2O$ specimen.

The $WO_3{\times}H_2O$ nanowhiskers do not show absorption in the 500−800 nm range (Figure 4a, A1); however, after the in situ formation of the nanowhiskers in the polycarbosilane-siloxane matrix (the c-$WO_{3-x}/WO_3{\times}H_2O/[-Si(O)CH_2-]_n$ nanocomposite), significant absorption in the 500−800 nm range is found (Figure 4a, B1). The absorption of the c-$WO_{3-x}/WO_3{\times}H_2O/[-Si(O)CH_2-]_n$ nanocomposite in the 500−800 nm range originates from W^{5+} species at the surfaces of the nanowhiskers, which absorb strongly in the visible range.[27,49,50] The presence of W^{5+} species is confirmed by X-ray photoelectron spectroscopy (XPS) measurements. W-4f (Figure 5a) and W-4d (Figure 5b) core-level photoelectron spectra are decomposed and fitted to W^{6+}, W^{5+}, and W^{4+} oxidation states (24%, 62%, and 14%, respectively). The W-4f binding energies are 34.4, 35.7, and 36.9 eV for W^{4+}, W^{5+}, and W^{6+}, respectively. The W-4d binding energies are 244.7, 247.1, and 249.1 eV for W^{4+}, W^{5+}, and W^{6+}, respectively. The W-4f and W-4d binding energies are slightly larger than those of the values reported in the literature.[51,52] The deviation and increase in the binding energies of metal oxide nanoparticles as compared to those of the bulk values have been attributed to the size effects.[53,54] Therefore, the surfaces of the nanowhiskers in the c-$WO_{3-x}/WO_3{\times}H_2O/[-Si(O)CH_2-]_n$ nanocomposite contain substoichiometric c-WO_{3-x}.

As expected, the c-$WO_{3-x}/[-Si(O)CH_2-]_n$ and c-WO_{3-x} specimens (Figure 4b, B2 and A2, respectively) absorb more strongly in the visible range, when compared to the c-$WO_{3-x}/WO_3{\times}H_2O/[-Si(O)CH_2-]_n$ and $WO_3{\times}H_2O$ specimens (Figure 4b, B1 and A1, respectively).

The results from an additional experiment indicate that the thermal treatment at 200 °C causes degradation of the polymeric matrix in the c-$WO_{3-x}/[-Si(O)CH_2-]_n$ nanocomposite. In this experiment, the nanowhiskers of the c-$WO_{3-x}/WO_3{\times}H_2O/[-Si(O)CH_2-]_n$ and c-$WO_{3-x}/[-Si(O)CH_2-]_n$ nanocomposites are dissolved in an aqueous ammonia solution. The dissolution and removal of the nanowhiskers are confirmed by XRD. The remaining matrix from the c-$WO_{3-x}/[-Si(O)CH_2-]_n$ specimen, which is thermally treated at 200 °C, shows significant absorption in the visible range (Figure 4b, Matrix-B2), while the remaining matrix from the c-$WO_{3-x}/WO_3{\times}H_2O/[-Si(O)CH_2-]_n$ sample, which is heat-treated at 120 °C, does not absorb in the same range (Figure 4b, Matrix-B1). This finding agrees with the results of STA-IR characterization, which indicates the decomposition of $[-Si(O)CH_2-]_n$ matrix at temperatures as low as 200 °C in the c-$WO_{3-x}/[-Si(O)CH_2-]_n$ nanocomposite.

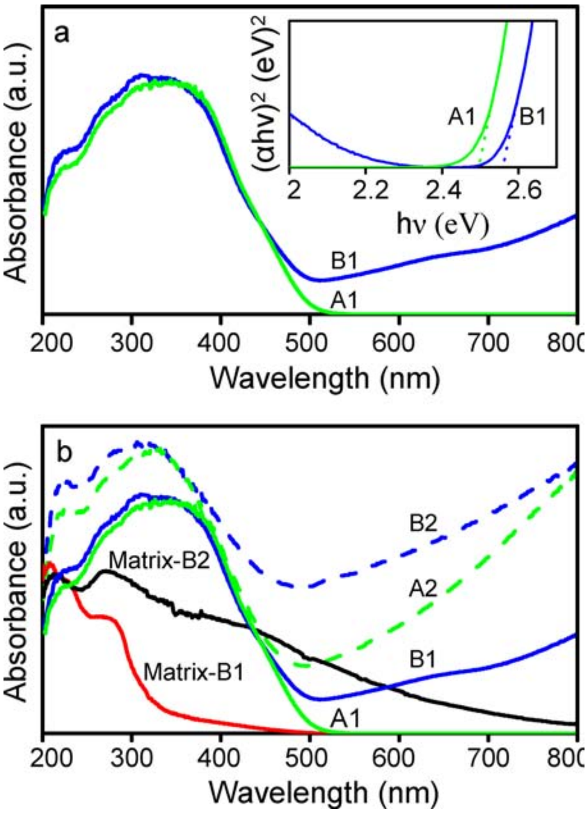

Figure 4. (a) DR-UV−vis spectra of $WO_3{\times}H_2O$ (green line, A1) and c-$WO_{3-x}/WO_3{\times}H_2O/[-Si(O)CH_2-]_n$ (blue line, B1) specimens. In the inset, the plot of $(\alpha h\nu)^2$ versus $h\nu$ is shown to determine E_g. (b) DR-UV−vis spectra of the above two specimens, green and blue lines, respectively, and after their thermal treatment at 200 °C under Ar atmosphere; c-WO_{3-x} (green dash line, A2) and c-$WO_{3-x}/[-Si(O)CH_2-]_n$ (blue dash line, B2) specimens, respectively. DR-UV−vis spectra of the remaining matrixes: Matrix-B1 (red line) and Matrix-B2 (black line) after the nanowhiskers are leached out from the c-$WO_{3-x}/WO_3{\times}H_2O/[-Si(O)CH_2-]_n$ and c-$WO_{3-x}/[-Si(O)CH_2-]_n$ specimens, respectively.

The polymeric matrix in the c-$WO_{3-x}/[-Si(O)CH_2-]_n$ nanocomposite absorbs significantly in the visible range, which makes c-$WO_{3-x}/[-Si(O)CH_2-]_n$ nanocomposite unsuitable for photocatalysis. Therefore, only the porosity and photocatalytic performance of the c-$WO_{3-x}/WO_3{\times}H_2O/[-Si(O)CH_2-]_n$ nanocomposite and the reference specimens, $WO_3{\times}H_2O$ and $[-Si(O)CH_2-]_n$, will be discussed.

Porosity Characteristics. The most remarkable features of the as-synthesized c-$WO_{3-x}/WO_3{\times}H_2O/[-Si(O)CH_2-]_n$

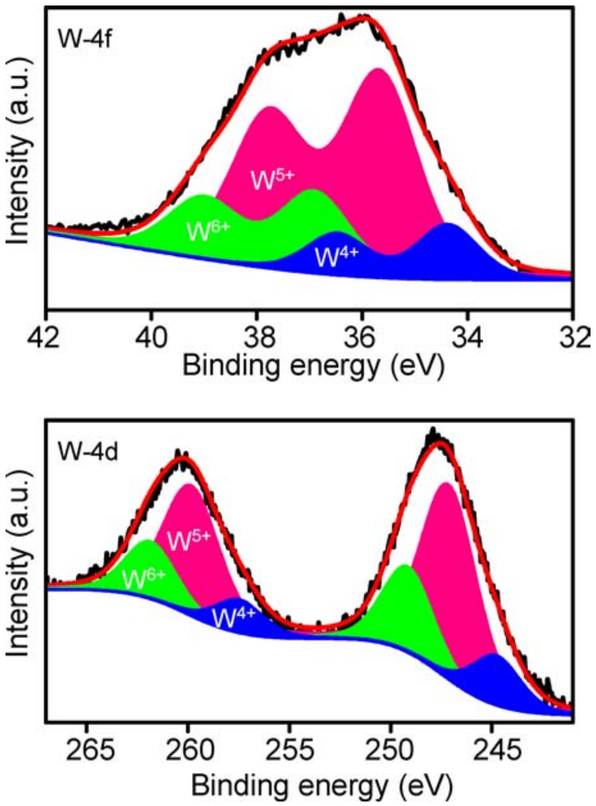

Figure 5. XPS spectra of c-$WO_{3-x}/WO_3\times H_2O/[-Si(O)CH_2-]_n$ nanocomposite, showing the decomposition and fitting of the W-4f and W-4d lines to W^{6+} (green), W^{5+} (pink), and W^{4+} (blue) oxidation states.

nanocomposite are the high volume of mesopores and the high specific surface area, as well as the high photocatalytic activity under visible light (Table 1).

Table 1. Porosity and Photocatalytic Activity Characteristics of $[-Si(O)CH_2-]_n$ (I), $WO_3\times H_2O$ (II), and c-$WO_{3-x}/WO_3\times H_2O/[-Si(O)CH_2-]_n$ (III) Specimens

characteristic	I	II	III
S_{BET} (m^2 g^{-1})[a]	655	40	509
S_{meso} (m^2 g^{-1})[b]	68	40	509
V_p (cm^3 g^{-1})[c]	0.41	0.27	1.11
V_{meso} (cm^3 g^{-1})[d]	0.09	0.27	1.11
r (nm)[e]	1.22	13.50	4.35
E_g (eV)		2.49	2.54
D_{eff}/D_{bulk}	0.31	0.90	0.72

[a] S_{BET}: specific surface area. [b] S_{meso}: mesoporous surface area. [c] V_p: total pore volume. [d] V_{meso}: mesoporous volume. [e] $r = 2V_p/S_{BET}$: average pore size.

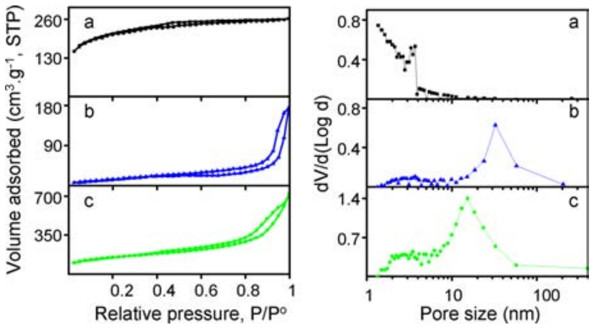

Figure 6. Nitrogen physisorption isotherms (left) and the corresponding pore size distributions (right) of $[-Si(O)CH_2-]_n$ (a), $WO_3\times H_2O$ (b), and c-$WO_{3-x}/WO_3\times H_2O/[-Si(O)CH_2-]_n$ (c) specimens.

The $[-Si(O)CH_2-]_n$ hybrid polymer reveals a type I nitrogen physisorption isotherm, which is typical for microporous materials. On the other hand, the c-$WO_{3-x}/WO_3\times H_2O/[-Si(O)CH_2-]_n$ nanocomposite exhibits type V nitrogen physisorption isotherm characteristic for mesoporous materials with type H3 loops, resulting from wedge-shaped or slit-shaped pores (Figure 6). Even if the specific surface area (S_{BET}) decreases slightly in the c-$WO_{3-x}/WO_3\times H_2O/[-Si(O)CH_2-]_n$ nanocomposite to 509 m^2 g^{-1}, if compared to that of the $[-Si(O)CH_2-]_n$ hybrid polymer (655 m^2 g^{-1}), this value is ~10 times larger than that of the $WO_3\times H_2O$ specimen (40 m^2 g^{-1}). In contrast to the $[-Si(O)CH_2-]_n$ hybrid polymer, the c-$WO_{3-x}/WO_3\times H_2O/[-Si(O)CH_2-]_n$ nanocomposite manifests a much higher mesopore volume, 1.11 versus 0.09 cm^3 g^{-1}, and a larger pore radius, 4.35 versus 1.22 nm, respectively.

The intriguing finding in our study is the transformation of the predominantly microporous $[-Si(O)CH_2-]_n$ hybrid polymer to completely mesoporous c-$WO_{3-x}/WO_3\times H_2O/[-Si(O)CH_2-]_n$ nanocomposite (Table 1, Scheme 2). This transformation could be understood, using the mechanism responsible for the mesostructuration of silica or various metal oxides with block copolymers.[23,55−57] In our case, after hydrolysis, the multivalent tungsten species form crown-type complexes with the hydrophilic Si−O−Si moieties as indicated in Scheme 2b, left. The result is the microphase separation of the hydrophilic Si−O−Si and hydrophobic $Si-CH_2-Si$ moieties, leading to the formation of a mesoporous structure in the c-$WO_{3-x}/WO_3\times H_2O/[-Si(O)CH_2-]_n$ nanocomposite (Scheme 2b, right), which is similar to the assembly of silica or metal oxides with block copolymers.[23,55−57]

The preferential association of tungsten species in the c-$WO_{3-x}/WO_3\times H_2O/[-Si(O)CH_2-]_n$ nanocomposite through crown-type complexes stabilized via physical (intermolecular) interactions is confirmed by ^{29}Si NMR spectroscopy. Because no new ^{29}Si NMR chemical shift signals are found in the c-$WO_{3-x}/WO_3\times H_2O/[-Si(O)CH_2-]_n$ nanocomposite as compared to those of the $[-Si(O)CH_2-]_n$ hybrid polymer (Figure 7), the formation of Si−O−W bonds is excluded. Therefore, the nanowhiskers are formed within the porous polycarbosilane-siloxane hybrid polymers without chemically reacting with the matrix.

On the contrary to the common ordered mesostructures,[23,55−57] a fast cross-linking happens within a few seconds after the addition of a 1 M HCl aqueous solution to the mixture of polydiethoxy carbosilane and tungsten(VI) oxychloromethoxide in methanol. Accordingly, polymerization and cross-linking processes dominate over a slower mesoscopic ordering. As a result, a nonordered mesoporous c-$WO_{3-x}/WO_3\times H_2O/[-Si(O)CH_2-]_n$ nanocomposite is obtained.

The thermal history for the synthesis of the c-$WO_{3-x}/WO_3\times H_2O/[-Si(O)CH_2-]_n$ and $WO_3\times H_2O$ specimens is the same. The high surface-to-bulk ratio of the nanowhiskers in the c-$WO_{3-x}/WO_3\times H_2O/[-Si(O)CH_2-]_n$ nanocomposite favors the dehydroxylation of the nanowhisker surfaces and the

Scheme 2. (a) Microporous $[-Si(O)CH_2-]_n$ Hybrid Polymer Made of 4-, 5-, 6-, 7-, and 8-Membered Silicon-Containing Ring Clusters, Resembling in This Way the Structure of Microporous Silica (See Refs 58,59); and (b) Preferential Association of Multivalent Tungsten Species in the $c\text{-}WO_{3-x}/WO_3{\times}H_2O/[-Si(O)CH_2-]_n$ Nanocomposite via Crown-type Complexes Stabilized by Physical (Intermolecular) Interactions

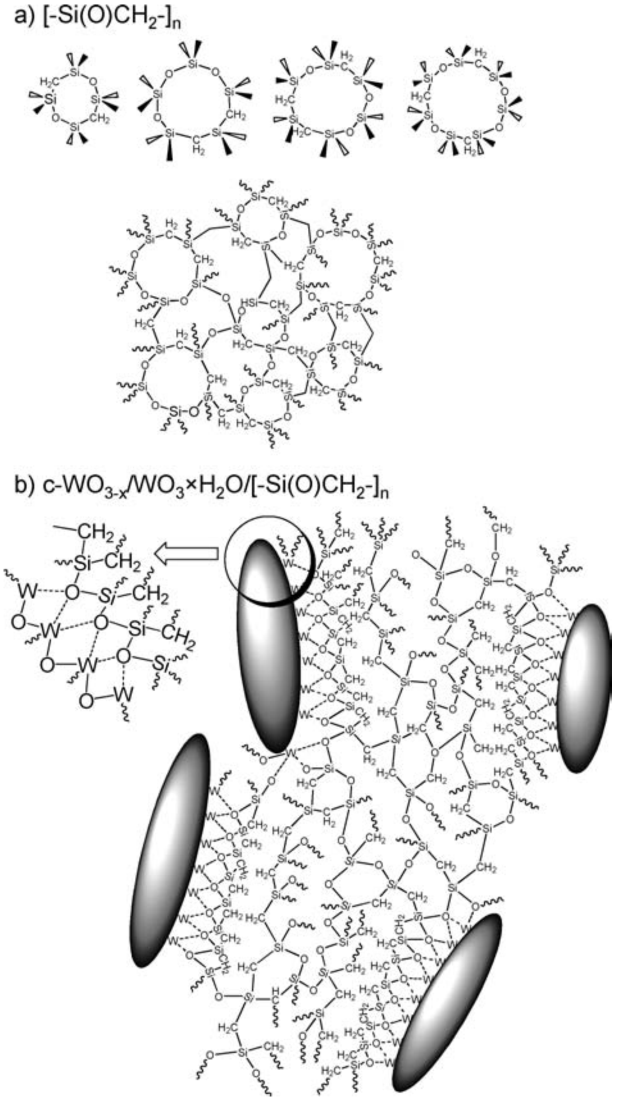

formation of substoichiometric $c\text{-}WO_{3-x}$, similar to the work by Cao et al.[32]

The preferential association of multivalent tungsten species via physical (intermolecular) interactions with oxygen atoms present in the matrix (Scheme 2b, left) leads to the enrichment of tungsten species on the surfaces of the nanowhiskers, inducing the formation of substoichiometric $c\text{-}WO_{3-x}$.

Photocatalytic Performance. The solar-driven photocatalytic activities of the $[-Si(O)CH_2-]_n$, $WO_3{\times}H_2O$, and $c\text{-}WO_{3-x}/WO_3{\times}H_2O/[-Si(O)CH_2-]_n$ specimens are measured by monitoring the change in the optical absorption of methylene blue (MB) solution at 664 nm during its adsorption and photocatalytic degradation process in the dark and under visible-light irradiation (40 W xenon lamp, UV cutoff at 420 nm), respectively. The MB adsorption experiments in the dark demonstrate the accessibility of the surfaces of the nanowhiskers in the $c\text{-}WO_{3-x}/WO_3{\times}H_2O/[-Si(O)CH_2-]_n$ nanocomposite.

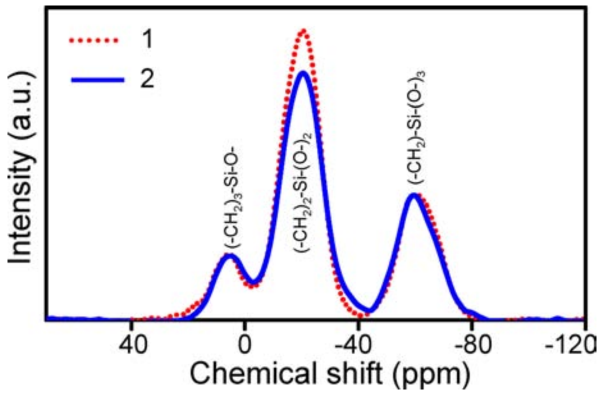

Figure 7. ^{29}Si NMR spectra of the $[-Si(O)CH_2-]_n$ (red dot, 1) and $c\text{-}WO_{3-x}/WO_3{\times}H_2O/[-Si(O)CH_2-]_n$ (blue, 2) specimens. The chemical shift signals related to $(-CH_2)_3-Si-O-$, $(-CH_2)_2-Si-(O-)_2$, and $(-CH_2)-Si-(O-)_3$ units at 3.4, −20, and −60 ppm, respectively, are indicated.

The effective diffusion (D_{eff}) for the molecules with radius r_m through the pores of radius r_p in polar solvents, such as water, is related to bulk diffusivity (D_B):[23]

$$\frac{D_{eff}}{D_B} = \frac{(1 - r_m/r_p)^2}{(1 + 2r_m/r_p)} \qquad (1)$$

Practically, a D_{eff}/D_B ratio larger than 0.70 is required for effective diffusion of molecules under study.[23] Taking r_m of the diffusing species (MB) as 0.36 nm, we obtain a D_{eff}/D_B equal to 0.31, 0.90, and 0.72 for the $[-Si(O)CH_2-]_n$, $WO_3{\times}H_2O$, and $c\text{-}WO_{3-x}/WO_3{\times}H_2O/[-Si(O)CH_2-]_n$ specimens, respectively. Hence, small pores in the $[-Si(O)CH_2-]_n$ hybrid polymer limit the diffusion of MB, whereas the pores in the $c\text{-}WO_{3-x}/WO_3{\times}H_2O/[-Si(O)CH_2-]_n$ nanocomposite are large enough for effective diffusion of MB. As the minimum pore size, allowing for the diffusion of MB, is about 2.6 nm,[60] the microporous $[-Si(O)CH_2-]_n$ hybrid polymer with very small pores (~1.22 nm) adsorbs only ~0.3% of the initial MB in the dark. In contrast, the mesoporous $WO_3{\times}H_2O$ and $c\text{-}WO_{3-x}/WO_3{\times}H_2O/[-Si(O)CH_2-]_n$ specimens adsorb a significantly larger amount of MB, that is, ~76% and 82%, respectively.

Although the surface area of the $c\text{-}WO_{3-x}/WO_3{\times}H_2O/[-Si(O)CH_2-]_n$ nanocomposite is much higher than that of the $WO_3{\times}H_2O$ specimen (Table 1), the amount of MB adsorbed after 1 h of equilibration in the dark is almost similar for both specimens. The following experiment is performed to understand the nature of the adsorption sites in the $c\text{-}WO_{3-x}/WO_3{\times}H_2O/[-Si(O)CH_2-]_n$ nanocomposite. The nanowhiskers are removed from the $c\text{-}WO_{3-x}/WO_3{\times}H_2O/[-Si(O)CH_2-]_n$ nanocomposite by treatment in an aqueous ammonia solution to obtain pure mesoporous polycarbosilane-siloxane matrix. Next, MB adsorption at equilibrium for the remaining matrix is measured under the same conditions as those of the adsorption stage in the dark, showing ~12% adsorption of MB. This result indicates that the nanowhiskers are the main sites for the adsorption of MB in the $c\text{-}WO_{3-x}/WO_3{\times}H_2O/[-Si(O)CH_2-]_n$ nanocomposite and the high surface area of the mesoporous polycarbosilane-siloxane matrix has much lower capacity to adsorb MB. In other words, the mesoporous matrix of the $c\text{-}WO_{3-x}/WO_3{\times}H_2O/[-Si(O)-$

$CH_2-]_n$ nanocomposite provides mesopores for the diffusion of MB to the surfaces of the nanowhiskers with a low contribution to the overall adsorption. The low adsorption is because of the low polarity of the $Si-CH_2-Si$ groups, and it reveals that the adsorption of MB on the surfaces of the nanowhiskers is not restricted by physical (intermolecular) bonding between the matrix and the surfaces of the nanowhiskers as described in Scheme 2b, left. Either the physical (intermolecular) bondings happen partially between the matrix and the surfaces of the nanowhiskers, allowing for sufficient adsorption sites for MB, or they can be exchanged (physical bonds are weak) with MB during the diffusion and adsorption process.

The equilibrium adsorption in the dark is measured for 1, 1.5, 2, and 3 h. No further decrease in the concentration of MB after 1 h of adsorption in the dark is detected. Accordingly, 1 h of equilibrium adsorption in the dark is considered to be appropriate to start the photodegradation of MB under visible light irradiation.

The kinetic data of MB photodegradation after equilibrium adsorption in the dark are shown in Figure 8. MB does not degrade on the $[-Si(O)CH_2-]_n$ and $WO_3 \times H_2O$ specimens during visible light irradiation, and the decrease in the equilibrium concentration of MB for these materials is similar to that of the blank run. In contrast, the c-$WO_{3-x}/WO_3 \times H_2O/[-Si(O)CH_2-]_n$ nanocomposite shows a 3-fold increase in the photocatalytic activity, leading to ~70% degradation of the MB after 3 h of irradiation.

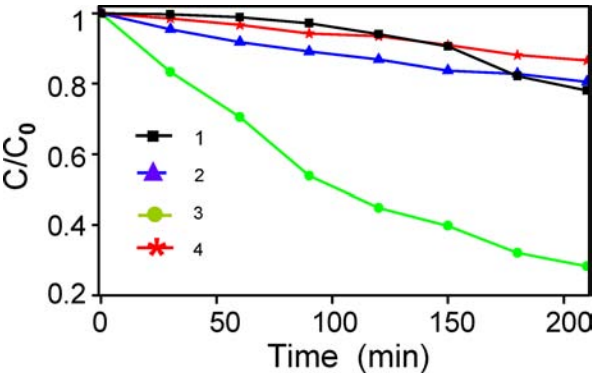

Figure 8. Degradation of MB after visible light irradiation ($\lambda > 420$ nm) by the $[-Si(O)CH_2-]_n$ (■, 1), $WO_3 \times H_2O$ (blue ▲, 2), and c-$WO_{3-x}/WO_3 \times H_2O/[-Si(O)CH_2-]_n$ (green ●, 3) specimens. A blank run (red ★, 4) for MB solution under visible light irradiation is measured for comparison, excluding the possibility of direct MB degradation during visible light irradiation of the c-$WO_{3-x}/WO_3 \times H_2O/[-Si(O)CH_2-]_n$ nanocomposite. MB concentration C during visible light irradiation is normalized by the equilibrium concentration of MB after 1 h of adsorption in the dark in each case, C_0.

Following the arguments presented in refs 1−3, we suggest that the dispersion of the nanowhiskers in the c-$WO_{3-x}/WO_3 \times H_2O/[-Si(O)CH_2-]_n$ nanocomposite increases the photocatalytic degradation of MB via the following mechanisms: (i) reducing the recombination rate of photogenerated electrons and holes, (ii) increasing the encounter between the photogenerated electrons (holes) with O_2 (MB), respectively, and (iii) formation of the c-$WO_{3-x}/WO_3 \times H_2O$ nanoheterostructures.

(i) Assuming the size of the c-$WO_{3-x}/WO_3 \times H_2O$ nanoheterostructures is comparable to Debye length of the tungsten oxide (~5 nm),[61] the minority carriers generated within a few nanometer from the surfaces of the nanowhiskers in the c-$WO_{3-x}/WO_3 \times H_2O/[-Si(O)CH_2-]_n$ nanocomposite would escape recombination and reach the oxidizable species.[62,63]

(ii) The high surface-to-bulk ratio of the nanowhiskers in the c-$WO_{3-x}/WO_3 \times H_2O/[-Si(O)CH_2-]_n$ nanocomposite increases the probability for the photocatalytic reactions at the surfaces of the nanowhiskers to occur. The surface-to-bulk ratio of the nanowhiskers in the c-$WO_{3-x}/WO_3 \times H_2O/[-Si(O)CH_2-]_n$ nanocomposite is 3 times larger than that of the $WO_3 \times H_2O$ specimen. Therefore, the nanowhiskers in the c-$WO_{3-x}/WO_3 \times H_2O/[-Si(O)CH_2-]_n$ nanocomposite provide a shorter path for the diffusive transport of electrons and holes to the surfaces of the nanowhiskers, making also the recombination of electrons and holes less probable.

(iii) It has been recently shown that cubic tungsten oxide formed by partial thermal decomposition of tungsten oxide monohydrate makes a heterostructure with the parent tungsten oxide monohydrate, resulting in a more efficient electron hole pair separation and enhanced photocatalytic degradation of organic dyes.[32] Therefore, c-$WO_{3-x}/WO_3 \times H_2O/[-Si(O)CH_2-]_n$ nanocomposite contains well-dispersed nanowhiskers, which are actually nanoheterostructures between c-WO_{3-x} and $WO_3 \times H_2O$, providing an efficient photocatalyst.

Although tungsten oxide and its hydrates offer the possibility to harvest the visible range of solar light,[12,64] the use of these materials for the photocatalytic degradation of organic compounds has been hampered. The main reason for that is the low conduction band level of tungsten oxide, which is more positive than the oxidation/reduction potential (vs NHE, normal hydrogen electrode) required for the single-electron reduction of oxygen:

$$O_2 + e^- = O_2{}^-(aq), \qquad E_0 = -0.284 \text{ V}$$

$$O_2 + H^+ + e^- = HO_2(aq), \qquad E_0 = -0.046 \text{ V}$$

As a result, the consumption of photogenerated electrons and the subsequent oxidative degradation of organic pollutants by the holes are effectively reduced.[27,65] However, as shown recently for tungsten oxide, the photogenerated electrons can be involved in competitive multielectron reduction reactions of O_2, which is more positive than for the single-electron processes:[27,65]

$$O_2 + 2H^+ + 2e^- = H_2O_2(aq), \qquad E_0 = 0.682 \text{ V}$$

$$O_2 + 4H^+ + 4e^- = 2H_2O(aq), \qquad E_0 = 1.230 \text{ V}$$

These multielectron processes have been proven to be facilitated by a high electron flux that can be gained via a Pt cocatalyst dispersed on the surface of WO_3, which behaves as a pool of electrons for the multielectron reduction reactions of O_2.[27,65]

By analogy, in the c-$WO_{3-x}/WO_3 \times H_2O/[-Si(O)CH_2-]_n$ nanocomposite, (i) the reduced recombination rate of electrons and holes, (ii) the better accessibility of electrons for O_2 reduction reactions, and (iii) the formation of c-$WO_{3-x}/WO_3 \times H_2O$ nanoheterostructures could create a high flux of electrons needed for the multielectron reduction of O_2, enabling the efficient consumption of holes by the oxidizable species, resulting in the enhanced photocatalytic degradation of MB.

CONCLUSIONS

A novel approach is developed to disperse photocatalytically active nanoparticles in a hydrolytically stable mesoporous matrix. As demonstrated in the present case study, in situ formation of c-$WO_{3-x}/WO_3 \times H_2O$ nanoheterostructures in the $[-Si(O)CH_2-]_n$ matrix transforms the predominantly microporous $[-Si(O)CH_2-]_n$ hybrid polymer to completely mesoporous c-$WO_{3-x}/WO_3 \times H_2O/[-Si(O)CH_2-]_n$ nanocomposite, possessing high photocatalytic activity under visible light irradiation.

ASSOCIATED CONTENT

Ⓢ Supporting Information

Details of the synthesis and characterization methods, porosity optimization in the c-$WO_{3-x}/WO_3 \times H_2O/[-Si(O)CH_2-]_n$ nanocomposites, micro-Raman and FTIR spectra, band gap estimation, and elemental mapping. This material is available free of charge via the Internet at http://pubs.acs.org.

AUTHOR INFORMATION

Corresponding Author

mseifba@materials.tu-darmstadt.de

Notes

The authors declare no competing financial interest.

ACKNOWLEDGMENTS

Financial support by the priority program “Adapting surfaces for high temperature applications” (SPP 1299) of the German Research Foundation (DFG) is greatly acknowledged. R.R. thanks the Fonds der Chemischen Industrie, Frankfurt, Germany, for continuous financial support. M.H. is grateful to the Alexander von Humboldt Stifung for a postdoctoral fellowship.

REFERENCES

(1) Osterloh, F. E. *Chem. Soc. Rev.* **2013**, in press, DOI: 10.1039/c2cs35266d.

(2) Zheng, H. D.; Ou, J. Z.; Strano, M. S.; Kaner, R. B.; Mitchell, A.; Kalantar-Zadeh, K. *Adv. Funct. Mater.* **2011**, *21*, 2175.

(3) Pan, J. H.; Dou, H. Q.; Xiong, Z. G.; Xu, C.; Ma, J. Z.; Zhao, X. S. *J. Mater. Chem.* **2010**, *20*, 4512.

(4) Kamat, P. V. *J. Phys. Chem. C* **2007**, *111*, 2834.

(5) Van Hoecke, K.; Quik, J. T. K.; Mankiewicz-Boczek, J.; De Schamphelaere, K. A. C.; Elsaesser, A.; Van der Meeren, P.; Barnes, C.; McKerr, G.; Howard, C. V.; Van De Meent, D.; Rydzynski, K.; Dawson, K. A.; Salvati, A.; Lesniak, A.; Lynch, I.; Silversmit, G.; De Samber, B.; Vincze, L.; Janssen, C. R. *Environ. Sci. Technol.* **2009**, *43*, 4537.

(6) Simon-Deckers, A.; Loo, S.; Mayne-L'Hermite, M.; Herlin-Boime, N.; Menguy, N.; Reynaud, C.; Gouget, B.; Carriere, M. *Environ. Sci. Technol.* **2009**, *43*, 8423.

(7) Colvin, V. L. *Nat. Biotechnol.* **2003**, *21*, 1166.

(8) Ou, J. Z.; Rani, R. A.; Balendhran, S.; Zoolfakar, A. S.; Field, M. R.; Zhuiykov, S.; O'Mullane, A. P.; Kalantar-zadeh, K. *Electrochem. Commun.* **2013**, *27*, 128.

(9) Yang, J.; Li, W. Z.; Li, J.; Sun, D. B.; Chen, Q. Y. *J. Mater. Chem.* **2012**, *22*, 17744.

(10) Wei, W.; Shaw, S.; Lee, K.; Schmuki, P. *Chem.-Eur. J.* **2012**, *18*, 14622.

(11) Zhang, X. H.; Lu, X. H.; Shen, Y. Q.; Han, J. B.; Yuan, L. Y.; Gong, L.; Xu, Z.; Bai, X. D.; Wei, M.; Tong, Y. X.; Gao, Y. H.; Chen, J.; Zhou, J.; Wang, Z. L. *Chem. Commun.* **2011**, *47*, 5804.

(12) Jiao, Z. H.; Wang, J. M.; Ke, L.; Sun, X. W.; Demir, H. V. *ACS Appl. Mater. Interfaces* **2011**, *3*, 229.

(13) Hojamberdiev, M.; Prasad, R. M.; Morita, K.; Zhu, Y. F.; Schiavon, M. A.; Gurlo, A.; Riedel, R. *Appl. Catal., B: Environ.* **2012**, *115*, 303.

(14) Hojamberdiev, M.; Prasad, R. M.; Morita, K.; Schiavon, M. A.; Riedel, R. *Microporous Mesoporous Mater.* **2012**, *151*, 330.

(15) Tanaka, D.; Oaki, Y.; Imai, H. *Chem. Commun.* **2010**, *46*, 5286.

(16) Reddy, E. P.; Davydov, L.; Smirniotis, P. *Appl. Catal., B: Environ.* **2003**, *42*, 1.

(17) Ma, N.; Quan, X.; Zhang, Y. B.; Chen, S.; Zhao, H. M. *J. Membr. Sci.* **2009**, *335*, 56.

(18) Ma, N.; Fan, X. F.; Quan, X.; Zhang, Y. B. *J. Membr. Sci.* **2009**, *336*, 109.

(19) Choi, H.; Sofranko, A. C.; Dionysiou, D. D. *Adv. Funct. Mater.* **2006**, *16*, 1067.

(20) Fang, D.; Luo, Z. P.; Huang, K. L.; Lagoudas, D. C. *Appl. Surf. Sci.* **2011**, *257*, 6451.

(21) Higashimoto, S.; Ushiroda, Y.; Azuma, M. *Top. Catal.* **2008**, *47*, 148.

(22) Halaoui, L. I.; Abrams, N. M.; Mallouk, T. E. *J. Phys. Chem. B* **2005**, *109*, 6334.

(23) Li, L.; Krissanasaeranee, M.; Pattinson, S. W.; Stefik, M.; Wiesner, U.; Steiner, U.; Eder, D. *Chem. Commun.* **2010**, *46*, 7620.

(24) Bamwenda, G. R.; Arakawa, H. *Appl. Catal., A* **2001**, *210*, 181.

(25) Xi, G. C.; Yue, B.; Cao, J. Y.; Ye, J. H. *Chem.-Eur. J.* **2011**, *17*, 5145.

(26) Xiang, Q.; Meng, G. F.; Zhao, H. B.; Zhang, Y.; Li, H.; Ma, W. J.; Xu, J. Q. *J. Phys. Chem. C* **2010**, *114*, 2049.

(27) Abe, R.; Takami, H.; Murakami, N.; Ohtani, B. *J. Am. Chem. Soc.* **2008**, *130*, 7780.

(28) Xi, G. C.; Yan, Y.; Ma, Q.; Li, J. F.; Yang, H. F.; Lu, X. J.; Wang, C. *Chem.-Eur. J.* **2012**, *18*, 13949.

(29) Qiu, Y. C.; Xu, G. L.; Kuang, Q.; Sun, S. G.; Yang, S. H. *Nano Res.* **2012**, *5*, 826.

(30) Amano, F.; Li, D.; Ohtani, B. *Chem. Commun.* **2010**, *46*, 2769.

(31) Hong, S. J.; Jun, H.; Borse, P. H.; Lee, J. S. *Int. J. Hydrogen Energy* **2009**, *34*, 3234.

(32) Cao, J.; Luo, B. D.; Lin, H. L.; Xu, B. Y.; Chen, S. F. *Appl. Catal., B: Environ.* **2012**, *111*, 288.

(33) Liu, Y.; Xie, C. S.; Li, H. Y.; Chen, H.; Zou, T.; Zeng, D. W. *J. Hazard. Mater.* **2011**, *196*, 52.

(34) Zhao, Z. G.; Miyauchi, M. *Angew. Chem., Int. Ed.* **2008**, *47*, 7051.

(35) An, X. Q.; Yu, J. M. C.; Wang, Y.; Hu, Y. M.; Yu, X. L.; Zhang, G. J. *J. Mater. Chem.* **2012**, *22*, 8525.

(36) Wang, F. G.; Di Valentin, C.; Pacchioni, G. *J. Phys. Chem. C* **2012**, *116*, 8901.

(37) Wang, F. G.; Di Valentin, C.; Pacchioni, G. *ChemCatChem* **2012**, *4*, 476.

(38) Chang, X. T.; Sun, S. B.; Zhou, Y.; Dong, L. H.; Yin, Y. S. *Nanotechnology* **2011**, *22*, 265603.

(39) Liu, Y. Y.; Li, Y.; Li, W. Z.; Han, S.; Liu, C. J. *Appl. Surf. Sci.* **2012**, *258*, 5038.

(40) Nah, Y. C.; Paramasivam, I.; Hahn, R.; Shrestha, N. K.; Schmuki, P. *Nanotechnology* **2010**, *21*, 105704.

(41) Chang, M. T.; Chou, L. J.; Chueh, Y. L.; Lee, Y. C.; Hsieh, C. H.; Chen, C. D.; Lan, Y. W.; Chen, L. J. *Small* **2007**, *3*, 658.

(42) Ou, J. Z.; Balendhran, S.; Field, M. R.; McCulloch, D. G.; Zoolfakar, A. S.; Rani, R. A.; Zhuiykov, S.; O'Mullane, A. P.; Kalantar-zadeh, K. *Nanoscale* **2012**, *4*, 5980.

(43) Char, K.; Cho, E. B. *Chem. Mater.* **2004**, *16*, 270.

(44) Brinker, C. J.; Dunphy, D. R.; Singer, S.; Cook, A. W.; Smarsly, B.; Doshi, D. A. *Langmuir* **2003**, *19*, 10403.

(45) Bazarjani, M. S.; Kleebe, H. J.; Mueller, M. M.; Fasel, C.; Yazdi, M. B.; Gurlo, A.; Riedel, R. *Chem. Mater.* **2011**, *23*, 4112.

(46) Tsuru, T.; Kanezashi, M.; Yada, K.; Yoshioka, T. *J. Am. Chem. Soc.* **2009**, *131*, 414.

(47) Liu, Q.; Shi, W.; Babonneau, F.; Interrante, L. V. *Chem. Mater.* **1997**, *9*, 2434.

(48) Kuti, L. M.; Bhella, S. S.; Thangadurai, V. *Inorg. Chem.* **2009**, *48*, 6804.

(49) Romanyuk, A.; Steiner, R.; Marot, L.; Oelhafen, P. *Sol. Energy Mater. Sol. Cells* **2007**, *91*, 1831.
(50) Hollinger, G.; Duc, T. M.; Deneuville, A. *Phys. Rev. Lett.* **1976**, *37*, 1564.
(51) Ranjbar, M.; Mahdavi, S. M.; Zad, A. I. *Sol. Energy Mater. Sol. Cells* **2008**, *92*, 878.
(52) Romanyuk, A.; Steiner, R.; Marot, L.; Oelhafen, P. *Sol. Energy Mater. Sol. Cells* **2007**, *91*, 1831.
(53) Parra, R. D.; Farrell, H. H. *J. Phys. Chem. C* **2009**, *113*, 4786.
(54) Zhao, Z. J.; Liu, F.; Qiu, L. M.; Zhao, L. Z.; Yan, S. K. *Acta Phys.-Chim. Sin.* **2008**, *24*, 1685.
(55) Lee, J.; Orilall, M. C.; Warren, S. C.; Kamperman, M.; Disalvo, F. J.; Wiesner, U. *Nat. Mater.* **2008**, *7*, 222.
(56) Zhao, D. Y.; Feng, J. L.; Huo, Q. S.; Melosh, N.; Fredrickson, G. H.; Chmelka, B. F.; Stucky, G. D. *Science* **1998**, *279*, 548.
(57) Yang, P. D.; Zhao, D. Y.; Margolese, D. I.; Chmelka, B. F.; Stucky, G. D. *Nature* **1998**, *396*, 152.
(58) Hacarlioglu, P.; Lee, D.; Gibbs, G. V.; Oyamaa, S. T. *J. Membr. Sci.* **2008**, *313*, 277.
(59) Oyama, S. T.; Lee, D.; Hacarlioglu, P.; Saraf, R. F. *J. Membr. Sci.* **2004**, *244*, 45.
(60) Houas, A.; Lachheb, H.; Ksibi, M.; Elaloui, E.; Guillard, C.; Herrmann, J. M. *Appl. Catal., B: Environ.* **2001**, *31*, 145.
(61) Hoa, N. D.; El-Safty, S. A. *Nanotechnology* **2011**, *22*, 485503.
(62) Mor, G. K.; Shankar, K.; Paulose, M.; Varghese, O. K.; Grimes, C. A. *Nano Lett.* **2005**, *5*, 191.
(63) vandeLagemaat, J.; Plakman, M.; Vanmaekelbergh, D.; Kelly, J. J. *Appl. Phys. Lett.* **1996**, *69*, 2246.
(64) Gratzel, M. *Nature* **2001**, *414*, 338.
(65) Irie, H.; Miura, S.; Kamiya, K.; Hashimoto, K. *Chem. Phys. Lett.* **2008**, *457*, 202.